Journal of
Composites Science

MDPI

Article

A Study on the Relationship Between the Pore Characteristics of High-Performance Self-Compacting Concrete (HPSCC) Based on Fractal Theory and the Function of the Water–Binder Ratio (W/C)

Guihong Xu [1,*], Mingwei He [1,*], Li He [1], Yongsheng Chen [2], Li Duan [1] and Weiguo Jiao [1]

[1] School of Civil Engineering, Guizhou Institute of Technology, Guiyang 550001, China; lihe@git.edu.cn (L.H.); lduan1987@163.com (L.D.); 20150701@git.edu.cn (W.J.)
[2] China Railway 11th First Group Third Engineering Co., Ltd., Shiyan 442000, China; cyscsn@163.com
* Correspondence: enjoymentanne@163.com (G.X.); 20160712@git.edu.cn (M.H.)

Abstract: The mechanical properties of High-Performance Self-Compacting Concrete (HPSCC) are strongly influenced by its pore structure, but the impact of varying water–binder ratios (W/C) on this relationship remains unclear. To address this, the present study investigates HPSCC with W/C ratios ranging from 0.19 to 0.23, aiming to elucidate the connection between pore structure, fractal characteristics, and mechanical performance. Through a combination of compressive strength testing, low-temperature nitrogen adsorption, and Scanning Electron Microscopy (SEM) observations, this study reveals key insights. First, compressive strength initially increases with a decreasing W/C ratio but plateaus beyond W/C = 0.21, identifying an optimal range for balancing strength and workability. Second, the pore structure of HPSCC is characterized by cylindrical, ink-bottle, and planar interstitial pores, with significant fractal characteristics. Notably, the fractal dimension decreases as the W/C ratio increases, indicating reduced pore complexity and improved homogeneity. Finally, a strong linear correlation ($R^2 > 0.9$) between the W/C ratio, fractal dimension, and compressive strength provides a predictive tool for assessing HPSCC performance. This study concludes that the internal pore structure is a critical determinant of HPSCC strength, and the identified optimal W/C ratio range offers guidance for mixture designs. Additionally, fractal dimension analysis emerges as a novel method to evaluate HPSCC's microstructural quality, enabling predictions of long-term performance and durability. These findings contribute to the scientific basis for designing high-performance concrete materials with improved mechanical properties and durability.

Keywords: C80 high-performance self-compacting concrete (HPSCC); micropore; fractal dimension; compressive strength; water–binder ratio (W/C)

Academic Editors: Ying-Liang Chen and Pai-Haung Shih

Received: 3 December 2024
Revised: 13 January 2025
Accepted: 20 January 2025
Published: 2 February 2025

Citation: Xu, G.; He, M.; He, L.; Chen, Y.; Duan, L.; Jiao, W. A Study on the Relationship Between the Pore Characteristics of High-Performance Self-Compacting Concrete (HPSCC) Based on Fractal Theory and the Function of the Water–Binder Ratio (W/C). *J. Compos. Sci.* **2025**, *9*, 66. https://doi.org/10.3390/jcs9020066

1. Introduction

High performance self-compacting concrete (HPSCC) [1] has been widely applied in various projects such as tunnel engineering (e.g., Akashi Strait Bridge); bridge engineering (e.g., the first large-span water plate landscape bridge in Xinjiang); underwater concrete engineering (e.g., Jinhai Bridge in Zhuhai), high-speed railways [2] (CRTS III; filling layer of ballastless track structure); and super high-rise buildings [3].

HPSCC is a composite material with a complex structure due to the diversity of its constituent materials, the complexity of the application environment, and the randomness of the distribution of various material particles within the structure. This complexity leads to a large number of structurally discontinuous and irregularly shaped micropores within

the hardened concrete, which significantly affect the mechanical properties and durability of the material. The problem lies in understanding and optimizing the internal pore structure distribution characteristics of HPSCC, particularly when using machine-made sand and carbonate rock aggregates from the southwest region of China, which have not been extensively studied [4,5].

As shown in Figure 1, the classification of pores varies depending on different measurement methods and research techniques. Figure 2 illustrates the methods for determining and classifying pore structures.

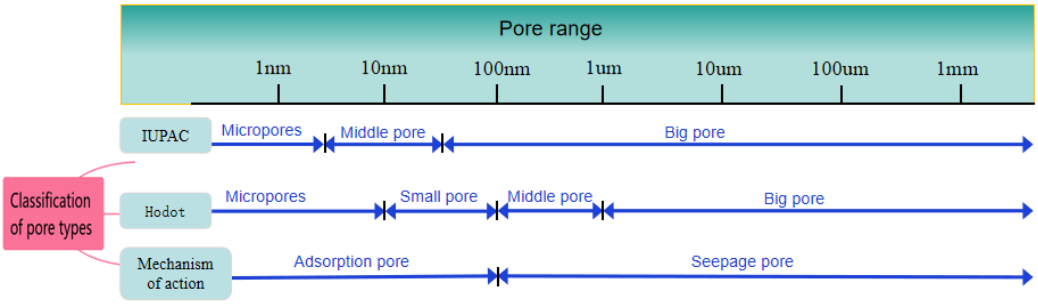

Figure 1. Classification of pore types. (Figure 1: The International Union of Pure and Applied Chemistry, abbreviated as "IUPAC", is an internationally recognized standard for pore size classification proposed by the International Union of Pure and Applied Chemistry [6]. The "Hodot" classification method was a coal pore size classification scheme proposed by the Soviet scholar Khodot (Ходот, B.B.) in 1966 [6]).

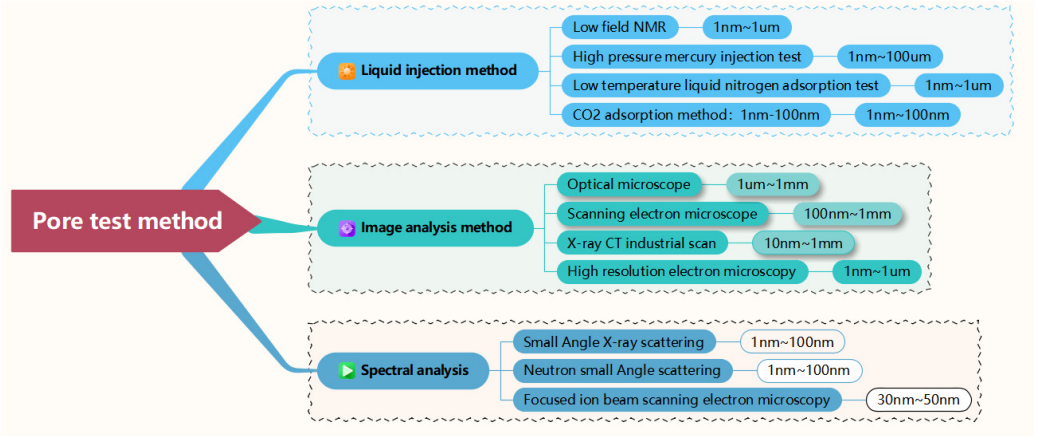

Figure 2. Pore structure determination method.

Current testing methods of concrete pore characteristics include scanning electron microscopy, X-ray CT [7,8], the mercury intrusion method [9], the linear wire method and the area ratio method, and the magnetic resonance imaging analysis technique [10]. By testing the porosity of concrete, researchers have tried to establish the relationship between such parameters as porosity distribution [11] and compressive strength [12], as well as frost resistance and durability. Yang et al. [13] used low-field magnetic resonance imaging analysis techniques and found that the porosity of concrete increases with an increase in sand content and initial air content. Cai, P. et al. [14], using a high-resolution X-ray CT and image processing, created a 3D pore structure model to analyze macropores (>0.15 mm). Their study found that approximately 80% of macropores fall within the 0.15–1 mm range, with a pore coordination number mostly within 20. The permeability anisotropy index was found to be mainly above 1, reaching up to 8. The permeability of M-RAPC is significantly correlated with macropore parameters, including effective porosity, tortuosity, and fractal dimensions. Hua C et al. [15] studied the effects of curing temperatures and the substitution

of molybdenum tailings on self-compacting concrete. The results show that higher curing temperatures and an optimal content of molybdenum tailings reduced porosity and radon emissions, indicating an improved microstructural density. Cui, Jinyang et al. [16] found that the porosity of SUHPC is higher than that of UHPC with the same fiber content (1.5%), due to air bubbles being trapped by high viscosity, leading to the formation of macropores in the hardened SUHPC matrix. Deng, G. et al. [17] studied pore structure changes and sulfate attacks in high-volume slag mortars under different curing conditions. Their study found that cement and slag hydration decrease porosity and the most probable pore diameter (MPPD), refining the mortar's pore structure. S. Du, Y. Zhang [18] found that adding GHB improves the pore structure of recycled aggregate concrete after high-temperature treatment, reducing pore distortion caused by high temperatures.

Fractal theory evolved from fractal geometry. Concrete, as an engineering material, displays a series of fractal characteristics both in its formation and in its working process. Many scholars use fractal theory to study this problem, so as to predict the structural failure characteristics or to analyze the mechanical properties of a structure. Jiao Chujie [19] et al. studied the fractal characteristics of high-strength concrete after dynamic damage and then characterized the fractal extension law of cracks based on fractal geometry theory using fractal dimensions and multifractal spectra. SHANG Xiaoyu [20] used the Photoshop CS6 image processing software to extract the internal damage cracks of materials and then characterized the fractal extension law of the cracks based on fractal geometry theory using fractal dimensions and multifractal spectra.

Despite these advancements, there is a research gap concerning the internal pore structure distribution characteristics of HPSCC, especially when prepared with machine-made sand and carbonate rock aggregates from the southwest region of China. This gap is significant, as the specific composition and environmental conditions of this region may lead to unique challenges in optimizing the pore structure and, consequently, the performance of HPSCC.

To address this research gap, a novel approach is proposed, which combines advanced imaging techniques, such as high-resolution X-ray CT and 3D reconstruction, with fractal theory to quantitatively study the development process of surface cracks in HPSCC. This study's solution involves the development of a comprehensive model that not only characterizes the fractal extension law of cracks but also incorporates the specific material properties and environmental conditions of HPSCC prepared with machine-made sand and carbonate rock aggregates from the southwest region of China. The novelty of this approach lies in its ability to predict structural failure characteristics and to analyze the mechanical properties of HPSCC with unprecedented accuracy, offering a significant advancement in the optimization of HPSCC's performance and durability.

2. Sample Preparation

2.1. Experimental Materials

The materials required for preparing the HPSCC experiment included cement, carbonate rock-based manufactured sand, carbonate rock-based gravel, slag powder, silica fume, microspheres, an expansive agent, a water reducer, etc.

The cement was P.O 42.5, produced by "Luzhou Said Cement Co., Ltd." (Luzhou, China), with a standard consistency of 26.8%, an initial setting time of 125 min, a final setting time of 223 min, an average value of mortar fluidity of 210 mm, representative values of flexural strength at 7 days of 6.1 MPa, and a compressive strength of 33.8 MPa.

The flexural strength of this cement at 28 days was 7.6 MPa, and the compressive strength was 50.7 MPa. Tested [21,22] by the Guizhou Provincial Building Materials Product Quality Inspection and Testing Institute (Guiyang, China), its various chemical elements are listed in Table 1.

Table 1. Mineral composition and content of cement.

Test Items	SO_3	SiO_2	Fe_2O_3	Al_2O_3	CaO	MgO	CL^-	K_2O	Na_2O	P_2O_5
Test results	2.5%	18.2%	4.3%	6.2%	62.2%	1.5%	NO	1.01%	0.31%	0.2%

To improve the strength of the concrete and to reduce the amount of cementitious material, two sizes of crushed stone as coarse aggregates were selected for this experiment. The first type was gravel with a diameter ranging from 5 mm to 10 mm, and the second type of crushed stone had a diameter between 10 mm to 16 mm. The test results are shown in Table 2. According to [23], the harmful substances contained in the crushed stone were tested, and the results are shown in Table 3.

Table 2. Record of gravel quality inspection.

Test Items	Particle Size Distribution				Average Mud Content	Average Needle-Like Particles	Average Value of Crushing Index	The Average Content of Soil	Average Compressive Strength of Carbonate Parent Rock
Small diameter "Guarnite"	Nominal diameter (mm) of sieve pore	2.5	5.0	10.0	0.6%	1.5%	7.6%	0.2%	75.8 MPa
	Score remaining%	17.2	76.9	3.9					
	Cumulative screen surplus%	98.0	80.8	3.9					
Large diameter "Gravel"	Nominal diameter of sieve pore (mm)	5	10	16	0.7%	1.8%	7.7%	0.2%	71.5 MPa
	Score remaining%	4.9	92.3	1.9					
	Cumulative screen surplus%	99.1	94.2	1.9					

Table 3. Testing results of hazardous substances in large diameter "crushed stone".

Test Items	Technical Requirements	Technical Requirements	Test Results	Conclusions
Chloride ion content		≤0.06%	0.01%	Meets the requirements
Harmful substances	Sulphide and sulfate content (converted to SO_3 by mass)	≤1.0%	0.2%	Meet the requirements
	Organic matter content in pebbles (colorimetric test)	The color should not be darker than the standard color. Otherwise, strength comparison tests should be conducted according to the method for cement mortar strength tests, and the compressive strength ratio should not be less than 0.95.	Qualified	

The manufactured sand used in the experiment was prepared by the Guizhou Panshi Building Materials Company (Bijie, China), and the results of an inspection by the Guizhou Building Materials Quality Inspection and Testing Institute (Guiyang, China) are shown in Table 4.

Before conducting the experiment, the fineness modulus, mud content, and stone powder content of the "manufactured sand" were measured, with specific data detailed in Table 5. Additionally, the grading sieve residue and cumulative sieve residue of the manufactured sand were measured, with the results presented in Figures 3–5.

Table 4. "Machine-made sand" testing results.

Test Items		Technical Requirements	Test Results	Conclusions
Chloride ion content		≤0.06%	0.01%	Meets the requirements
Harmful substances	Sulphide and sulfate content (converted to SO_3 by mass)	≤1.0%	0.2%	Meet the requirements
	Organic matter content (tested by colorimetry)	Color should not be darker than standard color. Otherwise, a strength contrast test should be carried out according to the cement mortar strength test method, and the compressive strength ratio should not be less than 0.95.	Qualified	
	Mica content	≤2%	0.1%	
	Light substance content	≤1%	0.3%	

Table 5. "Machine-made sand" test record.

Test Items	Modulus of Fineness	Moisture Content	The Average Content of Soil	Stone Powder Content MB Average ($g \cdot kg^{-1}$)	Crushing Index
Test results	3.0	2.2%	0.3%	7.7%	14%

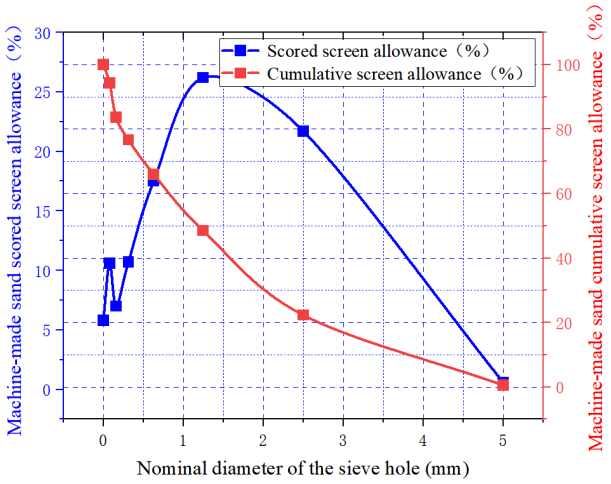

Figure 3. Scored screen allowance and cumulative screen allowance of machine-made sand.

The slag powder used in the experiment was provided by Guizhou "Guixin Building Materials Co., Ltd." (Guiyang, China). The silica fume, microspheres, and expansive agent used in the experiment were provided by China Railway 11th Bureau Group Co., Ltd. (Shiyan, China). According to [21,24], the samples were randomly selected and submitted to the Guizhou Building Materials Quality Inspection and Testing Institute (Guiyang, China) for testing. The fineness (specific surface area) of the slag powder was 462 m^2/kg, and the results of the mineral composition test are shown in Table 6. The particle size distribution of the slag powder was analyzed by a laser particle size analyzer, as shown in Figures 4 and 5.

The fineness (specific surface area) of the silica fume was 883.5 m^2/kg, with an average particle size of 2.515 m^2/kg. The particle size distribution is shown in Figures 4 and 5. The remaining results are shown in Table 6.

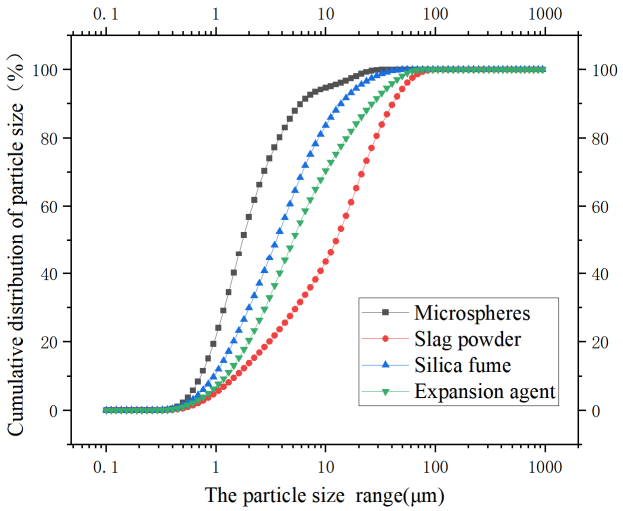

Figure 4. Diagram of particle size cumulative distribution.

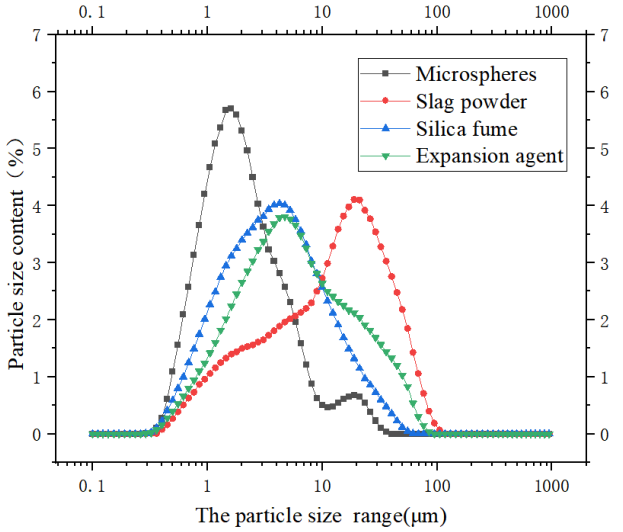

Figure 5. Particle size distribution.

Table 6. Mineral composition and content of slag powder.

Test Items	SO_3	SiO_2	Fe_2O_3	Al_2O_3	CaO	MgO	CL^-	K_2O	Na_2O	P_2O_5
Slag powder	2.7%	24.2%	3.2%	16.7%	37.8%	7.5%	No	1.2%	No	0.2%
Silica fume	0.7%	92.1%	0.2%	0.8%	0.2%	0.5%	No	0.3%	No	0.04%
Microspheres	0.4%	64.4%	5.4%	10.2%	10.0%	1.1%	No	2.6%	0.7	0.7%

The fineness of the microspheres (specific surface area) was 1520 m^2/kg, and the mineral composition is shown in Table 6. The particle size distribution of the microspheres was analyzed by a laser particle size analyzer, as shown in Figures 4 and 5. The fineness of the expansive agent was 672.8 m^2/kg, the content of MgO was 1.4%, and the content of alkali was 0.05%. The particle size distribution of the expansive agent is shown in Figure 5.

Based on the performance requirements of HPSCC, considering the performance of raw materials and the adaptability of cement, this experiment used polycarboxylate-based admixtures (self-formulated) to adjust the state of the paste. In accordance with regulations [25,26], the samples were randomly selected and tested, with the test results shown in Table 7.

Table 7. Ingredients and contents of admixtures.

Test Items	Chloride Ion Content	Alkali Content	Solid Content	Density	PH	Na_2SO_4
Test results	No	0.35%	24.9%	1.04%	5.6%	0.1%

2.2. Mix Proportion Design of HPSCC

The design strength grade of the HPSCC was C80, the designed density was 2400 kg/m^3, the sand ratio was 0.47, and the water–binder ratio (W/C) ranged from 0.19 to 0.21. The mix design is shown in Table 8.

Table 8. C80 HPSCC mix design (kg/m^3).

	Sand Rate	W/C	Machine-Made Sand/kg	Total Amount of Cementitious Material					Gravel/kg	Crushed Stone/kg	Polycarboxylic Admixture
				Cement/kg	Microspheres/kg	Slag Powder/kg	Silica Fume/kg	Expansive Agent/kg			
HPSCC-A	0.47	0.19	620	380	62	76	70	32	367	551	2.8% of cementitious material
HPSCC-B	0.47	0.20	620	380	62	76	70	32	367	551	
HPSCC-C	0.47	0.21	620	380	62	76	70	32	367	551	
HPSCC-D	0.47	0.22	620	380	62	76	70	32	367	551	
HPSCC-E	0.47	0.23	620	380	62	76	70	32	367	551	

2.3. Experimental Sample

The sample dimensions were 100 mm × 100 mm × 100 mm, and the work was conducted at the laboratory of the Panshi Building Materials Laboratory in Bijie City, China. According to [27], the physical properties of the concrete mixture, determined by techniques such as the expansion plate test, J-ring test, V-type funnel test, and L-box test, are shown in Figure 6.

(**a**) Slump flow test: used to measure the fluidity of concrete paste

(**b**) J-ring test: used to test the ability of concrete slurry through a narrow space

(**c**) V-type funnel test: used to test the stickiness and anti-segregation of concrete slurry

(**d**) L-box test

(**e**) Sample casting

(**f**) Completed samples ("娄" refers to the name of the person conducting the experiment, "7–15" refers to the date, "A,B," refers to the serial number, "C80" refers to the strength grade of the sample.)

Figure 6. HPSCC experimental samples' preparation process.

3. Experimental Method

3.1. Compressive Strength

According to the national standard [28], for the samples that underwent standard curing for 28 days, a microcomputer-controlled hydraulic pressure testing machine YAW-2000B (100 kN) was used to measure compressive strength in this experiment, and the test speed was 0.5 MPa/S.

3.2. Low-Temperature Liquid Nitrogen Adsorption Experiment

The samples were cut into cubes of about 1 cm^3, and a low-temperature liquid nitrogen adsorption test was carried out with the BSD-PS1/2 series automatic BET analyzer. The weight of a sample was about 2~5 g. Before the low-temperature liquid nitrogen adsorption test, the samples were degassed at 200 °C for 120 min to remove internal impurities.

The samples were then placed in an adsorption station at a low temperature (liquid nitrogen, 77.3 K), and a certain amount of an adsorbent gas (N_2) was introduced into the sample tube under a relative pressure of $0.01 \leq P/P_0 \leq 0.995$. The N_2 adsorption/desorption isotherms were obtained by increasing or decreasing the adsorption equilibrium pressure of the adsorbent gases.

The specific surface area was calculated using the Brunauer–Emmett–Teller (BET) multi-molecular layer adsorption model, and the pore volume, average aperture distribution, total volume distribution, and average pore size were calculated through the Barrett–Joyner–Halenda (BJH) theory and gas isothermal adsorption curves. The lower limit for a specific surface-area measurement by the BET analyzer was 0.0005 m^2/g, with no upper limit, and the range for testing the average aperture was 0.35 to 500 nm.

3.3. Scanning Electron Microscope (SEM) Observations

To study the microstructural characteristics of the concrete, this paper utilized scanning electron microscopy (SEM) technology to conduct detailed observations of the pore structure parameters and the size and shape of the solidified material grains within the HPSCC.

The samples that underwent curing for 28 days were selected for slicing and polishing, and their micro-morphology, using a scanning electron microscope, was observed by using a field emission detector (resolution: 0.8nm; acceleration voltage: 0.2–30 kV; magnification: 35–900,000 times; detector: ETD\TLD\CBS; continuous rotation angle: R = 360 degrees).

4. Experiment Results and Discussion

4.1. Compressive Strength Result Analysis

This study produced five samples for each mix ratio of the HPSCC material and determined their compressive strength after standard curing for 28 days. During the tests, the loading speed was uniformly set to 0.5 MPa/s. Specific experimental data can be found in Table 9. It should be particularly noted that samples with a compressive strength variation exceeding 15% [28] in the test results were excluded from the statistical analysis.

According to Table 9, some samples had large errors, which may be caused by the following reasons: (1) Mold issues: deformation of the mold, uneven diagonals, and size tolerance can lead to uneven, irregular, contaminated, and porous surfaces on the formed samples, affecting the compressive strength test results of the concrete. (2) Material non-uniformity: this leads to deviations in compressive strength, which is an inevitable issue. (3) Improper operation by testing personnel. (4) Human operation errors: improper operations during the testing process, such as inaccurate placement of test blocks, particles, and dirt on the surface of the samples, can also affect the test results. (5) Testing equipment errors: insufficient precision of the testing equipment may also lead to deviations in test results.

Table 9. Compressive strength test results of HPSCC samples.

Sample Number	W/C	Compressive Strength of the Sample (MPa)	Samples with a Range Greater than 30% (MPa)	Standard Compressive Strength Value (MPa) f_c=0.95 $f_c^{'}$ [28]
HPSCC-A	0.19	98.3, 116.8, 108.2, 114.6, 78.9	78.9	104.00
HPSCC-B	0.20	119.9, 125.7, 98.1, 89.4, 101.3	89.4	105.08
HPSCC-C	0.21	101.4, 114.2, 71.6, 115.6, 118.6	71.6	106.82
HPSCC-D	0.22	102.3, 120.1, 97.6, 121.6, 120.1	NO	106.72
HPSCC-E	0.23	113.2, 110.7, 100.1, 111.9, 126.9	NO	106.93

4.2. Analysis of Pore Characteristics Based on Adsorption–Desorption Curve of Low-Temperature Liquid Nitrogen

The samples HPSCC-A, HPSCC-B, HPSCC-C, HPSCC-D, and HPSCC-E were cut to approximately 1 cm^3 in volume, respectively, and were then placed in a BET analyzer for a vacuum degassing treatment. The duration of the treatment was 120 min, with the degassing temperature set to 200 °C. After the degassing process was completed, the samples were transferred to an adsorption station for gas adsorption–desorption experiments. The experimental ambient temperature was controlled at 25.0 °C, with nitrogen (N_2) as the adsorbate, and the adsorption/desorption temperature was 77.3 K.

The adsorption/desorption curves of five different ratio samples are shown in Figures 7–11. The shape of the adsorption/desorption curves is related to the pore structure within the sample. Based on the shape of the adsorption–desorption isotherm curves, the structural shapes of the pores inside the samples under different equilibrium pressure conditions are roughly marked in this figure.

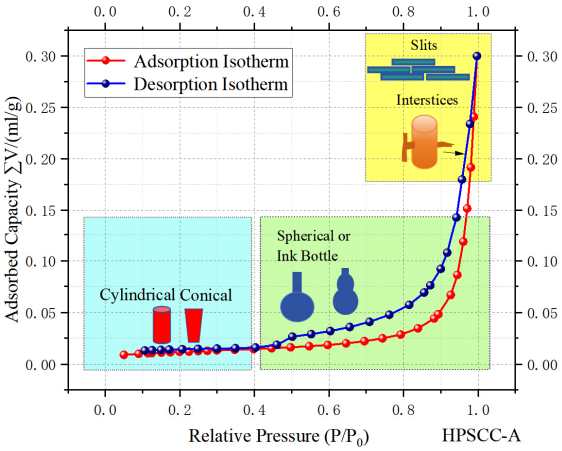

Figure 7. HPSCC-A adsorption/desorption isotherms. In the area of relatively low pressure ($P/P_0 < 0.45$), the curve rises slowly, and the adsorption and desorption curves coincide, indicating that the concrete is mainly composed of cylindrical pores and wedge-shaped pores. As the relative pressure increases, when $P/P_0 \geq 0.45$, the adsorption–desorption curve shows a separation, forming a large hysteresis loop, indicating that within this pressure range, the adsorbate mainly exists in the form of "ink-bottle" or "impermeable" pores. At the end of the curve, the adsorption–desorption curves tend to coincide, which indicates that the internal structure of the cementitious material has a "crack-pore" or "interstices" or "slit-like" particles formed in the plate. The adsorption capacity of the sample at the maximum relative pressure area is 0.3 mL/g.

From the structure of the adsorption/desorption isotherms in Figures 7–11, it can be seen that the adsorption/desorption isotherms of HPSCC belong to Type III. The isotherms can be roughly divided into two parts. The first part is the low-pressure region

at $0.8 < P/P_0$, where the isotherms increase slowly with a rise in pressure, indicating that within this range, as the pressure increases, the low-temperature N2 adsorption gradually transitions from monolayer adsorption to multilayer adsorption.

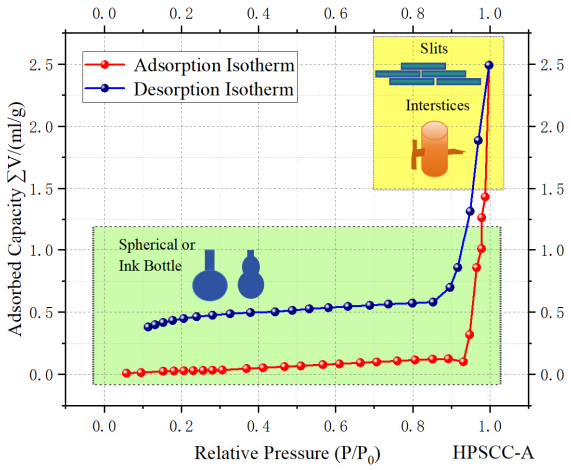

Figure 8. HPSCC-B adsorption/desorption isotherms. In the area of $P/P_0 < 0.93$, the curve rises slowly, and the adsorption and desorption curve are separated. This shows that the adsorbent in concrete does not completely dissociate; therefore, its pore shape is mainly "ink-bottle" and "spherical" air-tight pores. In the area of $0.93 \leq P/P_0 < 1$, the adsorption and desorption curves tend to coincide, suggesting that the sample has a "slit-like" structure formed by cracks or "interstices" particles inside.

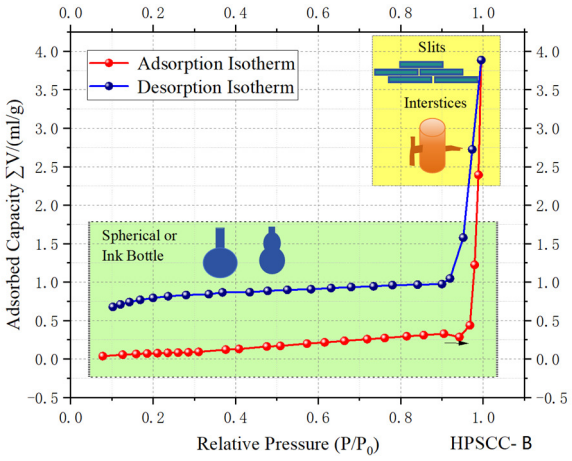

Figure 9. HPSCC-C Adsorption/desorption isotherms. The adsorption-desorption isotherms are similar to Figure 8. In the area of $P/P_0 < 0.93$, the sample is mainly composed of "ink-bottle" and "spherical" air-tight pores. At a relative pressure of $0.93 \leq P/P_0 < 1$, the sample has a "slit-like" structure formed by cracks or "interstices" particles inside.

In the second part, when $0.8 \leq P/P_0 < 0.99$, the isotherm presents a right-down bulge shape, and with an increase in the pressure, the adsorption capacity increases rapidly. The results show that the adsorption of liquid nitrogen in HPSCC at a low temperature is mainly the capillary condensation of mesoporous and macroporous.

In Figures 8 and 9, the adsorption/desorption curve separations show that the adsorbent does not separate completely after entering the pore interior. In Figure 7, Figure 10, and Figure 11, the adsorption/desorption curves form hysteresis loops at $0.4 \leq P/P_0 < 0.9$, indicating the presence of typical "ink-bottle" pores, unevenly distributed "tubular" pores with an average aperture, and closely packed "spherical particle interstitial" pores within the HPSCC samples.

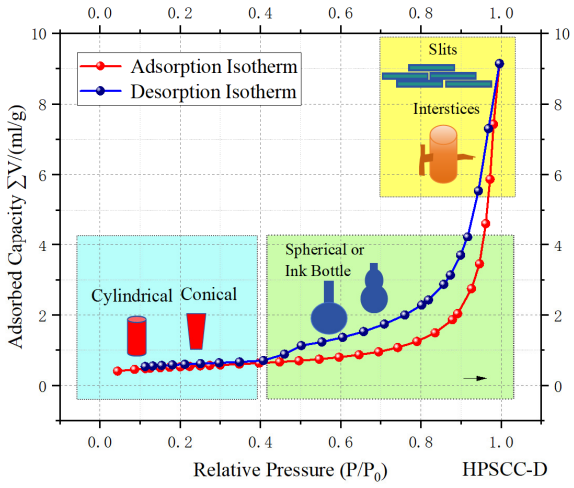

Figure 10. HPSCC-D adsorption/desorption isotherms. The adsorption–desorption isotherms are similar to Figure 11. Therefore, the pore structure is similar to that of HPSCC-A. The maximum adsorption capacity is 0.3 mL/g.

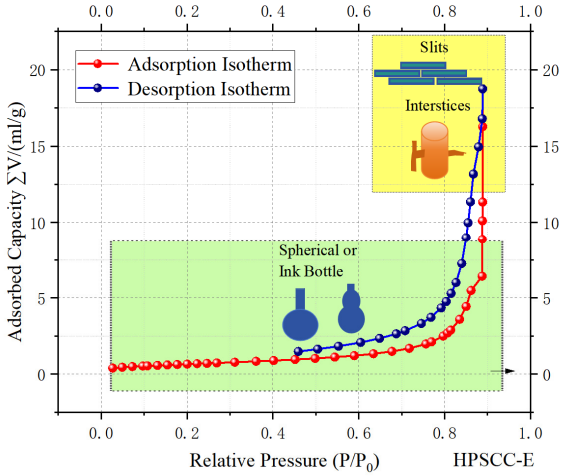

Figure 11. HPSCC-E adsorption/desorption isotherms. In the area of relatively low pressure ($P/P_0 < 0.42$), the experimental results only show the adsorption curve, indicating that within this pressure range, the adsorbate did not desorb and remained completely inside the pores. As the relative pressure increases, when $0.42 \leq P/P_0 < 0.8$, the adsorption–desorption curve shows a separation, and the adsorption pores mainly exists in the form of "ink-bottle" or "impermeable" pores. At the end of the curve ($0.8 \leq P/P_0 < 1$), the adsorption–desorption curves tend to coincide, which indicates that the internal structure of the cementitious material has a "crack-pore" or "interstices" or "slit-like" particles formed in the plate.

4.3. SEM MicroPore Morphology Analysis

The pore volume, pore size distribution, total volume distribution, and average pore size were calculated by the Barrett–Joyner–Halenda method, according to the adsorption/desorption isotherm curve, with aperture as the *X*-axis and the *Y*-axis representing the cumulative pore volume (located on the right and indicated by the blue curve) and the aperture/differential pore volume (located on the left and indicated by the red curve). The cumulative pore volume refers to the total volume of all pores within a specific aperture range, as determined by the BJH method analysis. The distribution of pores and fissures on the surface of the samples was observed by scanning electron microscopy, as shown in Figures 12–16.

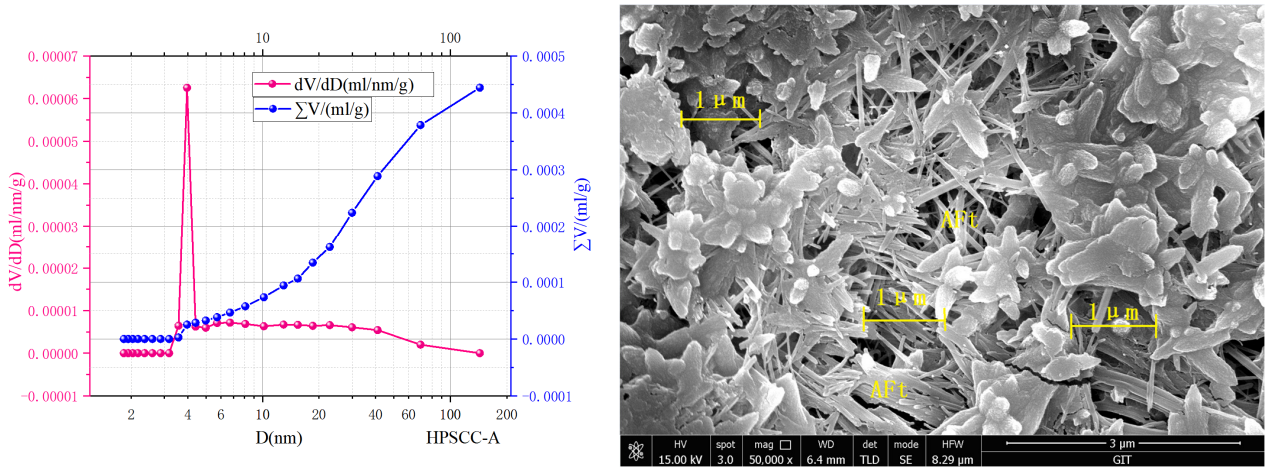

Figure 12. BJH (desorption) pore area and pore size curve and morphology.

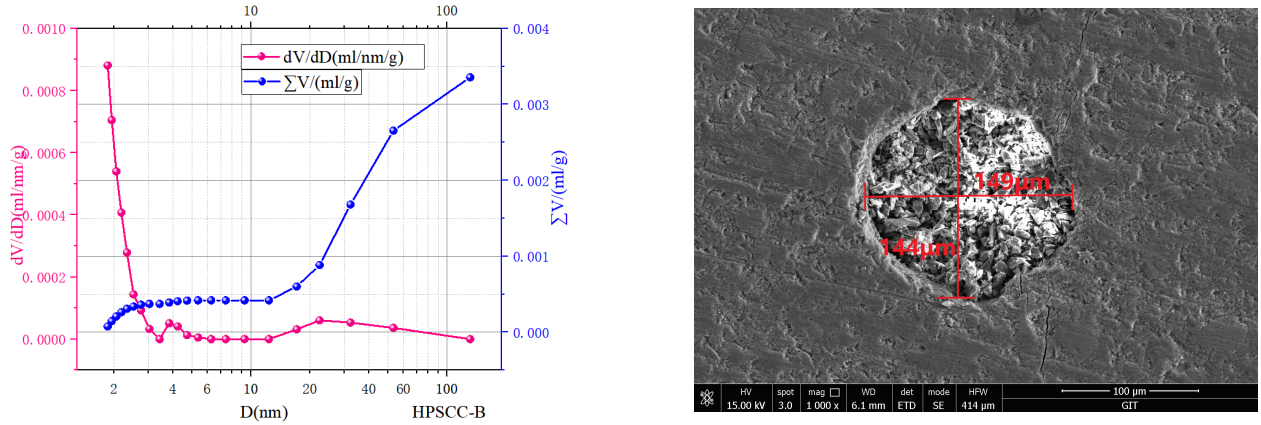

Figure 13. HPSCC-B BJH (desorption) pore area and pore size curve and Morphology.

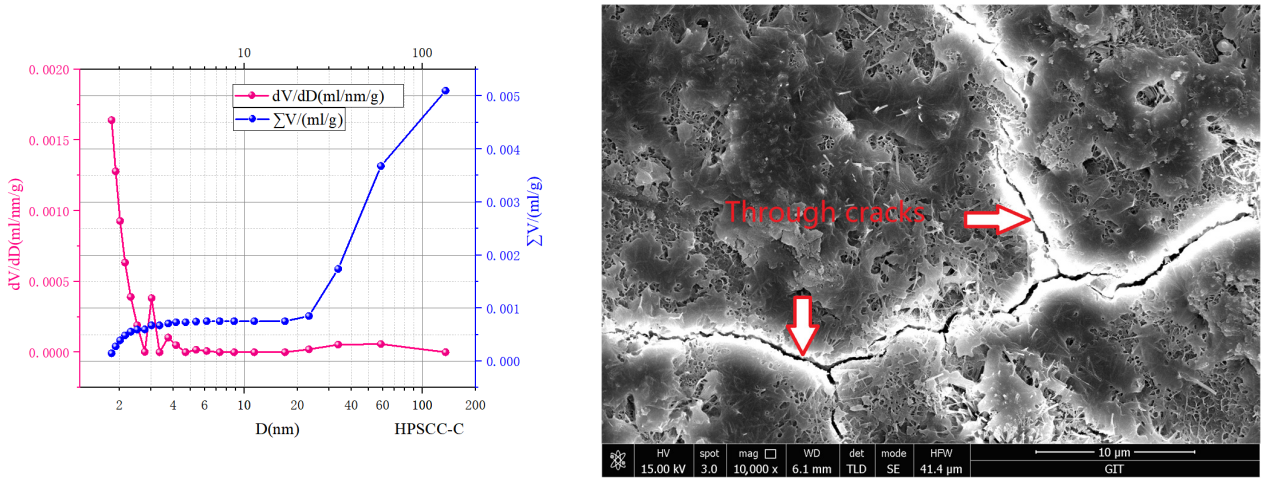

Figure 14. HPSCC-C BJH (desorption) pore area and pore size curve and morphology.

As can be seen from Figure 12, the cumulative pore volume of BJH was 0.0004 mL/g, the average pore diameter of BJH was 14.9115 nm, and the cumulative pore area was 0.1073 m^2/g. When the SEM image was magnified to 50kX, it was observed that a "needle-like" hydrated calcium sulphoaluminate (AFt) structure was connected with a "lilies-like" structure, and the whole structure was relatively compact, but there were still a lot of pores of about 1 μm. The pore shape and arrangement were complex and irregular. The variation

in the differential pore volume (dV/dD) reaches the highest point at about 3.9 nm, so the pore size distribution of the adsorbent is the most concentrated at 3.9 nm.

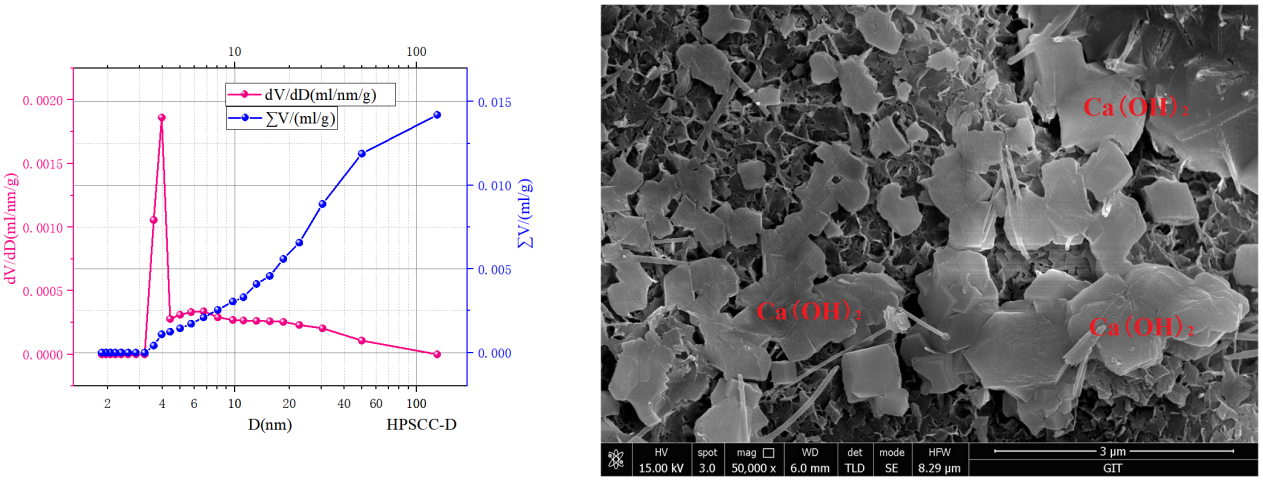

Figure 15. HPSCC-D BJH (desorption) pore area and pore size curve and morphology.

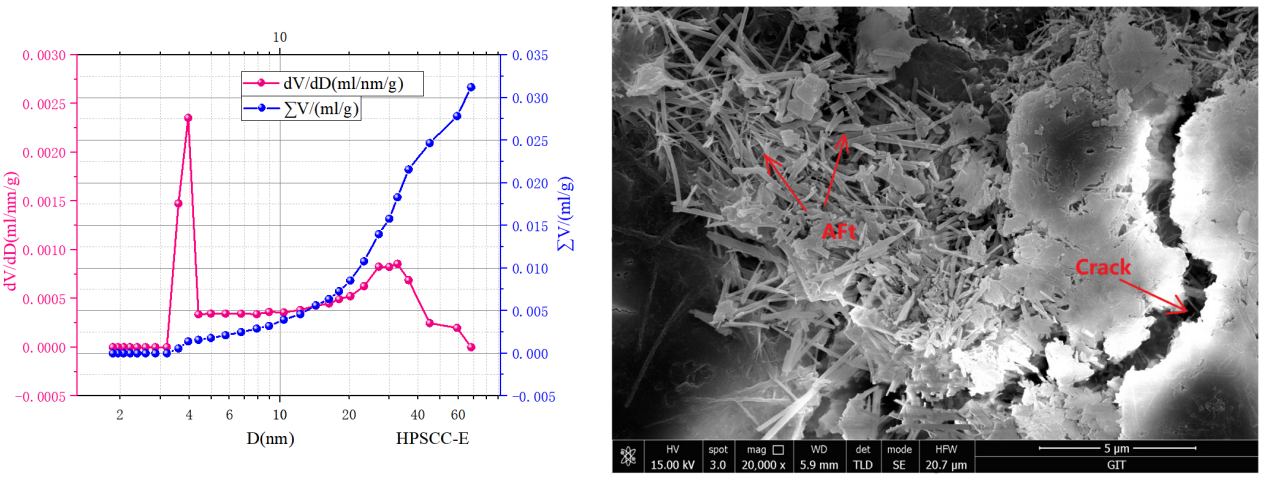

Figure 16. HPSCC-E BJH (desorption) pore area and pore size curve and morphology.

As can be seen from Figure 13, the accumulated pore volume of BJH was 0.0034 mL/g, the average pore diameter of BJH was 11.8498 nm, and the accumulated pore area was 1.1477 m^2/g. The differential pore volume curve (dV/dD) reaches the highest point at 1.86 nm, so the pore size distribution of the adsorbent is the most concentrated at 1.86 nm. So, a pore size of 1.86 nm is the largest proportion of all pore volumes. When the SEM image was magnified to 1000×, there were obvious pores. The diameter of the pores was about 144~149 µm, and the pore was approximately circular in shape.

As can be seen from Figure 14, the accumulated pore area was 1.8279 m^2/g, the accumulated pore volume was 0.0051 mL/g, and the average pore diameter was 11.1603 nm. The differential pore volume curve (dV/dD) reaches the highest point at 1.803 nm, so a pore size of 1.803 nm is the largest proportion of all pore volumes. When the sample was magnified by 10,000 times, it could be seen that there was a significant through-through fracture in the structure. The width of the fracture was about 0.5~1 µm, and the fracture surface continued to expand under the action of an external force, causing structural failure.

As can be seen from Figure 15, the accumulated pore area was 4.2487 m^2/g, the accumulated pore volume was 0.0142 mL/g, and the average pore diameter was 3.9606 nm. The differential pore volume curve (dV/dD) reaches the highest point at 3.9606 nm, so a pore size of 3.9606 nm is the largest proportion of all pore volumes. When magnified to

50 K at a selected point in the sample, "hexagonal-shaped" Calcium dihydroxide crystals ($Ca(OH)_2$) were observed. There were pores between the hexagonal crystals. Some "hexagonal" structures were associated with "needle-like" ettringite structures. The shape and arrangement of the pores were complex and irregular.

As can be seen from Figure 16, the accumulated pore area was 6.9400 m^2/g, the accumulated pore volume was 0.0312 mL/g, and the average pore diameter was 17.9827 nm. The differential pore volume curve (dV/dD) reaches the highest point at 3.9646 nm, so a pore size of 3.9646 nm is the largest proportion of all pore volumes. By scanning electron microscopy (SEM), it was found that primary cracks were obviously penetrated in the structure, and the width of the fracture was about 1 μm. It can also be observed that "needle-stick" ettringite structures and irregular sheet structures stick together next to the cracks, forming a crisscross stacking network.

It can be seen from Figures 12–16, there are a large number of pores, voids, and interpenetrating cracks in the HPSCC, which are mainly distributed in the range of 1–5 μm. The inner pores are mainly distributed in flaky minerals or mineral grains and are usually irregular or round in shape, often accompanied by cracks. The reason for the formation of a circular cavity is that the cementitious material is involved in the mixing process of air bubble formations that are caused. And the small bubbles will gather to form a larger bubble, and as a result, large voids are formed inside the solid structure.

4.4. Fractal Characteristics of Pores Based on Low-Temperature Liquid Nitrogen Adsorption Test

In this paper, the method of calculating the fractal dimension of the Frenkel–Halsey–Hill model proposed by Pfeifer P was used to process the data of liquid nitrogen adsorption. The Frenkel–Halsey–Hill model considers a gas adsorbed on a fractal surface, expressed in Formula (1):

$$\ln V = K \ln(\ln(p_0/p)) + C \quad (1)$$

In Formula (1), p is the equilibrium pressure; V is the volume of liquid nitrogen adsorption corresponding to the equilibrium pressure p; C and K are constants; K is a linear relationship coefficient, and the value of K is related to the adsorption mechanism; when the adsorption mechanism is capillary condensation, $K = D - 3$, where D is the fractal dimension; when the adsorption mechanism is a Van der Waals force action, ignoring the capillary action, $K = (D - 3)/3$.

There is a certain proportion relationship between fractal dimension and pore structure. The closer the fractal dimension is to 2, the more regular the pore surface, the simpler the pore structure, and the better the homogeneity. The closer the fractal dimension is to 3, the more irregular the pore surface is, the more complex the pore structure is, and the less homogeneous the pores are.

According to Figure 11, most of the test results show that when $0.4 < P/P_0$, the adsorption–desorption isotherm appears as a hysteresis loop, or the adsorption branch separates from the desorption branch. This is due to capillary condensation in the pores.

Therefore, adsorption data with $0.4 < P/P_0$ were selected as the object of analysis. Set $\ln(\ln(p_0/p))$ as the horizontal axis and $\ln V$ as the vertical axis. The test curves were fitted using the principle of least squares. The slope of the fitted line is K, and the fractal dimension value D can be obtained from the value of K.

As can be seen from Figures 17–21, the fractal dimension is between 2.3 and 2.5, and the experimental curve and the fitting curve are generally well correlated, both being close to 1. This indicates that the internal pores of the HPSCC gel structure have very good fractal characteristics.

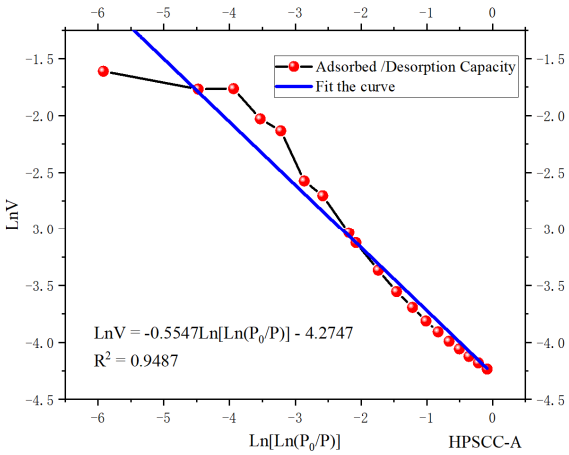

Figure 17. Low-temperature liquid nitrogen adsorption volume fractal dimension fitting diagram of HPSCC-A. The fitting equation is K = −0.55, the correlation coefficient R^2 is 0.95, and the fitting curve has a good correlation with the experimental curve. The fractal dimension D is 2.45.

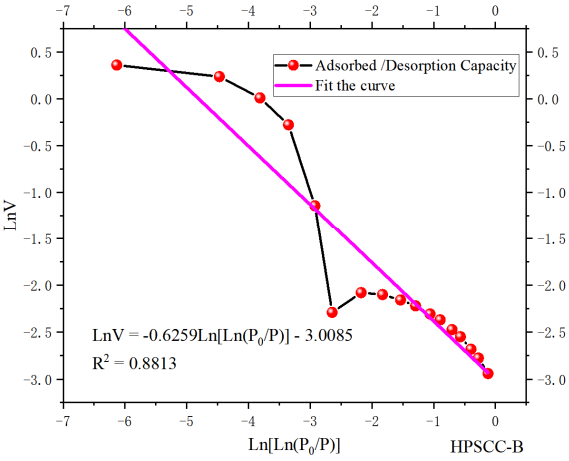

Figure 18. Low-temperature liquid nitrogen adsorption volume fractal dimension fitting diagram of HPSCC-B. The fitting equation is K = −0.63. Because the experimental curve fluctuates greatly, the correlation coefficient R^2 is 0.88. The fitting curve deviates from the experimental curve. The correlation coefficient R is a statistical index used to reflect the close degree of correlation between variables. It is generally considered that when $R^2 > 0.86$, the correlation between the two curves is good, and the fitting curve is acceptable. The fractal dimension D was calculated to be 2.37.

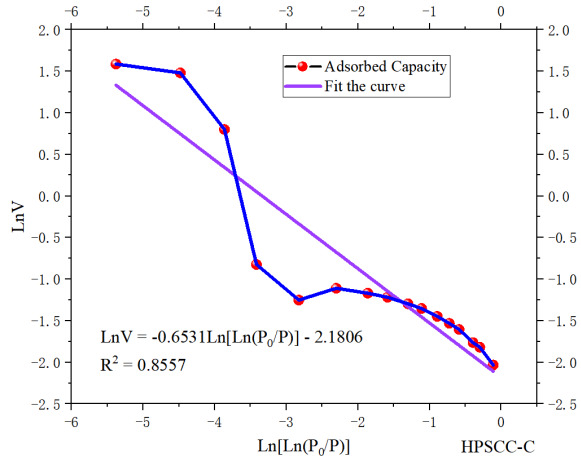

Figure 19. Low-temperature liquid nitrogen adsorption volume fractal dimension fitting diagram of HPSCC-C. The fitting equation is $K = -0.65$, the correlation coefficient R^2 is 0.87, and the fractal dimension D is 2.35.

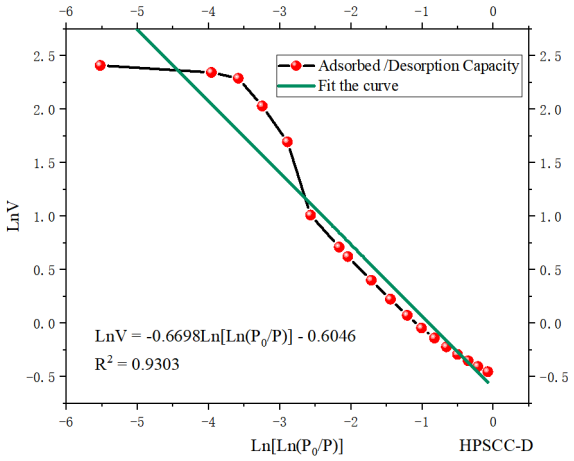

Figure 20. Low-temperature liquid nitrogen adsorption volume fractal dimension fitting diagram of HPSCC-D. The fitting equation is K = −0.67, the correlation coefficient R^2 is 0.93, and the fitting curve has a good correlation with the experimental curve. The fractal dimension D is 2.33.

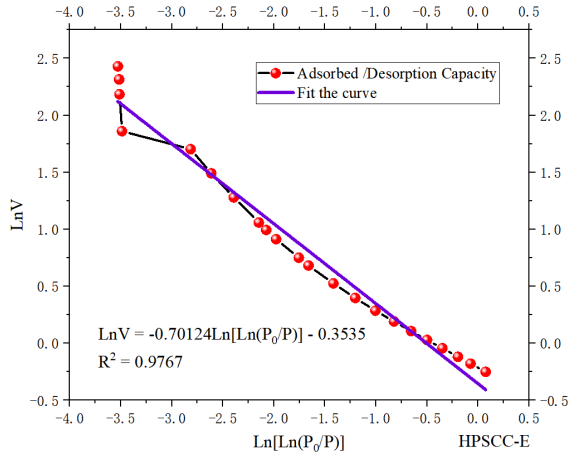

Figure 21. Low-temperature liquid nitrogen adsorption volume fractal dimension fitting diagram of HPSCC-E. The fitting equation is K = −0.70, the correlation coefficient R^2 is 0.977, and the fitting curve has a good correlation with the experimental curve. The fractal dimension D is 2.30.

As the water-to-cement (W/C) ratio gradually increases, the fractal dimension shows a decreasing trend, indicating that within the range of experimental tests, as the W/C increases, the complexity of the pore structure within the gel structure decreases, and the homogeneity of the pore distribution and pore structure improves.

4.5. Relationship Between Fractal Characteristics of Pores and W/C

The specific surface area, pore diameter, cumulative pore volume, and cumulative pore area, measured by the low-temperature liquid nitrogen adsorption test, were statistically analyzed, and the fractal dimension *D* was calculated according to the slope *K* of the equation fitted to Figure 8, as shown in Table 10.

Table 10. Summary of HPSCC experimental results.

Sample Number	W/C	Compressive Strength (MPa)	BJH Cumulative Pore Volume (mL/g)	BJH Average Pore Diameter (nm)	Cumulative Pore Area (m^2/g)	*K*	*D*	*R*
HPSCC-A	0.19	104.00	0.0004	14.9115	0.1073	−0.55	2.45	0.95
HPSCC-B	0.20	105.08	0.0034	11.8498	1.1477	−0.63	2.37	0.88
HPSCC-C	0.21	106.82	0.0051	11.1603	1.8279	−0.65	2.35	0.86
HPSCC-D	0.22	106.72	0.0142	13.3688	4.2487	−0.67	2.33	0.93
HPSCC-E	0.23	106.93	0.0312	17.9827	6.9400	−0.70	2.30	0.98

According to Table 10, a relationship between W/C and compressive strength, W/C and the BJH average pore size, the fractal dimension, and HPSCC compressive strength and a relationship between W/C and the fractal dimension can be established, as shown in Figures 22–25.

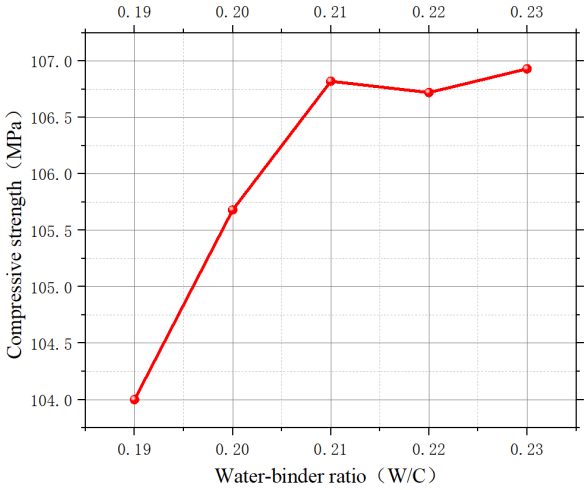

Figure 22. Relation between W/C and compressive strength.

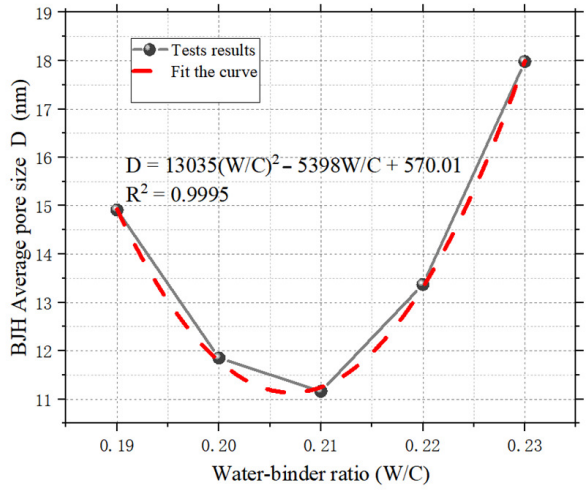

Figure 23. Relationship between W/C and BJH average pore size.

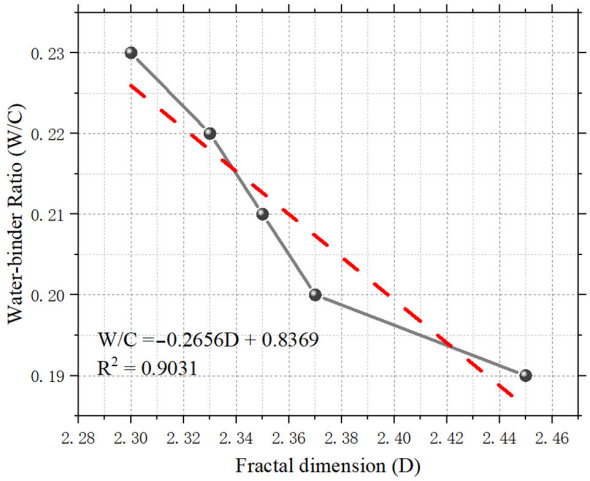

Figure 24. Relational curve between W/C and fractal dimension.

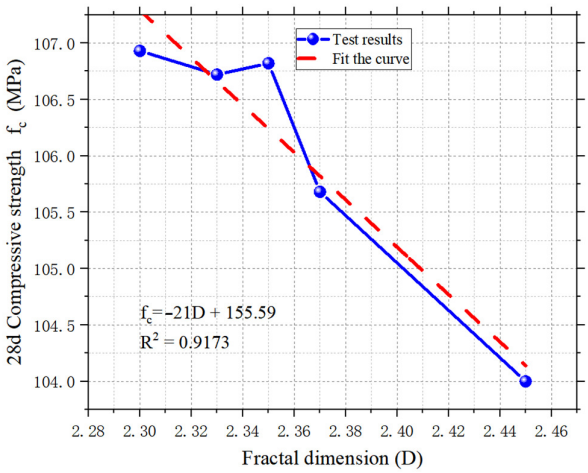

Figure 25. The relational curve between compressive strength and fractal dimension.

It can be seen from Figure 22 that as the water–binder ratio increases, the compressive strength of High-Performance Self-Consolidating Concrete (HPSCC) exhibits a positive correlation. However, within the range of W/C values of 0.21 to 0.23, the enhancement in compressive strength is minimal, suggesting that this interval represents an optimal mix where compressive strength reaches its peak. Within this optimal water-to-binder ratio range, the workability of the concrete is ensured, and its strength is maximized. This is of great significance for engineering practice, as it can help engineers optimize the use of materials while ensuring the safety of concrete structures and reducing costs.

It can be seen from Figure 23 that the relationship between the average pore size and W/C can be described by a quadratic function curve, with a correlation coefficient exceeding 0.99. When W/C is 0.21, the curve reaches its lowest point, indicating that the average pore size is the smallest and the pore structure is the most uniform at this point, thereby achieving the maximum compressive strength. By understanding and leveraging the quadratic relationship between the average pore size and water-to-binder ratio, engineers can optimize the mix proportions of concrete more effectively, enhancing the performance of the concrete. This has significant engineering implications for improving the safety, durability, and economy of engineering structures.

It can be seen from Figure 24 that the relationship between W/C and the fractal dimension can be represented by a linear function with a correlation coefficient of 0.9. The water–binder ratio of HPSCC has a good linear relationship with the internal pore fractal dimension. As the fractal dimension increases, the water–binder ratio decreases. This discovery reveals a significant linear correlation between the water-to-binder ratio of HPSCC and the fractal dimension of its internal pore structure. This relationship is of great importance for understanding and optimizing the microstructure of concrete.

It can be seen from Figure 25 that as the fractal dimension increases, the compressive strength decreases. This relationship can be represented by a linear function with a correlation coefficient of 0.92, indicating a good correlation. The fractal dimension, as an indicator of the complexity of the concrete pore structure, increases when the pore structure becomes more complex and irregular. This complex pore structure may lead to an uneven distribution of stress within the concrete, thereby reducing the overall performance of the material when subjected to compression. Consequently, as the fractal dimension increases, the compressive strength of the concrete decreases, possibly because more irregular pores provide sites for stress concentration, making the concrete more susceptible to failure under load.

5. Discussion

The present study provides a comprehensive analysis of the micropore characteristics of HPSCC with varying water–binder ratios (W/Cs), ranging from 0.19 to 0.23. The results offer valuable insights into the relationship between the internal pore structure of HPSCC and its mechanical properties, particularly compressive strength. This discussion will compare the findings with existing research and highlight the implications of these results for the field of concrete technology.

This study aligns with previous research that establishes a correlation between the W/C ratio and the compressive strength of concrete. Similar to the findings of Yang et al. [13] and Ye Linjie et al. [29], we observed an initial increase in the compressive strength with a decreasing W/C ratio, which is attributed to the denser microstructure and reduced porosity. However, the results also indicate a plateau in strength beyond a W/C ratio of 0.21, suggesting an optimal range for the W/C ratio in HPSCC. This finding is crucial for mix design optimization in HPSCC, as it balances the need for workability and strength.

An analysis of the pore structure using low-temperature nitrogen adsorption and SEM imaging revealed the presence of cylindrical pores, ink-bottle-shaped pores, and planar interstitial pores, which is consistent with the research by Cai et al. [14] on macropore structures in recycled aggregate pervious concrete. This study extends this understanding by quantifying the pore characteristics using fractal dimension analysis, providing a more nuanced view of the pore structure's impact on the mechanical properties of HPSCC.

The application of fractal theory to analyze the pore structure of HPSCC is a significant contribution of this study. The observed decrease in the fractal dimension with an increasing W/C ratio indicates a reduction in the complexity of the internal pore structure, which is supported by SEM observations. This finding is in line with the research by Jiao Chujie et al. [19] on the dynamic damage of high-strength concrete, where they used fractal theory to model damage evolution. This study further establishes the practical application of fractal theory in optimizing the W/C ratio for the improved performance of HPSCC.

This study reveals a strong linear relationship between the W/C ratio, fractal dimension, and compressive strength, with correlation coefficients above 0.9. This is a significant finding, as it provides a quantitative tool for predicting the compressive strength of HPSCC based on its pore structure. This relationship complements the work of Deng et al. [17] on the pore structure evolution of slag-blended mortars, as this study provides a broader understanding of the role of the W/C ratio in pore structure and strength development.

The findings of this study have profound implications for the production and application of HPSCC. The optimal W/C ratio range identified in this study can guide practitioners in formulating HPSCC mixtures that balance strength and workability. Moreover, the fractal dimension analysis provides a new method for assessing the microstructural quality of HPSCC, which can be used to predict long-term performance and durability.

In conclusion, this study contributes to our understanding of the microstructural characteristics of HPSCC and their relationship with compressive strength. The results provide a scientific basis for the design and application of HPSCC, emphasizing the importance of considering the internal pore structure in the development of high-performance concrete materials. Future research can build on these findings to explore the impact of other factors, such as aggregate type and curing conditions, on the microstructure and performance of HPSCC.

6. Conclusions

The intrinsic reasons for the damage failure and deterioration of the mechanical properties of HPSCC lie in the deformation of the internal pore structure and the expansion and penetration of microcracks caused by long-term environmental loads.

This process is closely related to the internal structural morphology and the condition of the pore distribution. In this study, crushed sand and gravel from carbonate rocks were used as coarse aggregates to prepare C80-grade high-strength self-compacting concrete. By combining the observation methods of specific surface area pore size analyzers and scanning electron microscopes (SEM), an experimental investigation into the internal pore structure and distribution characteristics of HPSCC was conducted based on fractal theory, and the following conclusions were drawn:

(1) This study completed experiments on the mix proportions of five different HPSCC samples with water–binder ratios (W/C) ranging from 0.19 to 0.23 and tested their compressive strength. The experimental results indicate that as the water–binder ratio gradually increased, the compressive strength of the HPSCC gel gradually increased. However, after W/C = 0.21, there was no significant improvement in compressive strength. The optimal W/C value for HPSCC was found to be between 0.21 and 0.23.

(2) The analysis results of the adsorption/desorption isotherms indicate that there is a large number of cylindrical pores, impermeable ink-bottle-shaped pores, and plate-like slit structures formed by a few flaky particles in HPSCC.

(3) The SEM scanning results indicate that the internal surface of the HPSCC is uneven with numerous primary crack pores, cavities, or through-going fissure structures. The width of the fissures is approximately between 1 to 5 μm, and the diameter of the microvoids is about 3 to 10 μm. Under an external force, the first possible rupture surface may form along these microcracks, affecting the structural mechanical properties.

(4) The pore structure of HPSCC exhibits distinct fractal characteristics, which can be quantitatively described by the fractal dimension. With an increase in the W/C, the fractal dimension shows a decreasing trend. When the W/C is between 0.21 and 0.23, as the water-to-cement ratio increases, the complexity of the pores within the HPSCC structure decreases, and the homogeneity of the pore distribution and pore structure improves, thereby enhancing the compressive strength of the HPSCC samples.

(5) There is a quadratic function curve relationship between W/C and the BJH average pore size, a linear function relationship between W/C and the fractal dimension, and a good linear relationship between compressive strength and the pore fractal dimension, with correlation coefficients all above 0.9.

Thus, it is evident that the fractal dimension value can not only quantitatively express the distribution of HPSCC pore structures but can also estimate the strength of HPSCC through the fractal dimension. Fractal theory provides a new perspective and tool for the analysis of concrete pore structures, which helps to deepen our understanding of the relationship between the microstructure and macroscopic properties of concrete and has important theoretical and practical applicational value for improving the performance and durability of concrete.

Author Contributions: G.X.: writing—review and editing, writing—original draft, and conceptualization. M.H.: writing—review and editing, writing–original draft, formal analysis, and conceptualization. L.H. and Y.C.: writing—review and editing, software, and resources. L.D.: writing—review and editing, methodology. W.J.: writing—review and editing, investigation, and data curation. All authors have read and agreed to the published version of the manuscript.

Funding: This research was funded by The Natural Science Foundation of Guizhou Province [Grant number: QIAN KE HEJICHU-ZK [2022]-027, ZK [2022]-170], the National Natural Science Foundation of China [Grant number: 52268065 and 52268053], and the Guizhou Province innovative high-level talent project [Grant number: QIAN KE HE Platform Talents-GCCQIAN KE [2023]053]. Thanks to Guizhou Yuanyuan Building Materials Co., Ltd. (Bijie, China) and Guizhou Province Rail Transit Infrastructure Operation & Maintenance (OM) and Digital Twin Applications (DTA) Team for their experimental support.

Data Availability Statement: The data presented in this study are available on request from the corresponding author due to requirements of the cooperative company.

Conflicts of Interest: Authors Yongsheng Chen is employed by the company China Railway 11th First Group Third Engineering Co., Ltd. The remaining authors declare that the research was conducted in the absence of any commercial or financial relationships that could be construed as a potential conflict of interest.

References

1. Yin, J.; Zhou, S. Application of High-Performance Concrete and Self-Compacting Concrete in Foreign Bridges. *Foreign Highw.* **2000**, *4*, 52–54. [CrossRef]
2. Wu, J.; Lin, H. Research and Application of Ultra-High Performance Concrete and Ultra-High Performance Self-Compacting Concrete. *Constr. Build. Mater. Decor.* **2010**, *11*, 46–50.
3. Arriagada, C.; Navarrete, I.; Lopez, M. Understanding the effect of porosity on the mechanical and thermal performance of glass foam lightweight aggregates and the influence of production factors. *Constr. Build. Mater.* **2019**, *228*, 116746. [CrossRef]
4. Akcay, B.; Sengul, C.; Tasdemir, M.A. Fracture behavior and pore structure of concrete with metakaolin. *Adv. Concr. Constr.* **2016**, *4*, 71–88. [CrossRef]
5. Zhang, Z.F.; Xu, G.H.; Li, Z.X.; Duan, L.; Jia, Y.; Liu, Z.H. Experimental Study on Micropore Structure of High-Performance Self-Compacting Concrete Prepared with Carbonate Rock Mechanism Sand and Stone. *Concrete* **2024**, *56*, 108–116. [CrossRef]
6. Yang, M.; Liu, L.; Liu, J.; Mao, J.; Cai, P. A Joint Characterization Study of the Pore Structure of Medium-Rank Coal by Nitrogen Adsorption-Mercury Intrusion-Nuclear Magnetic Resonance. *Coal Sci. Technol.* **2021**, *49*, 67–74.
7. Jiang, N.; Yuan, J.; Xu, X.L.; Zhang, S.L. Analysis of Pore Classification and Characterization in Shale Gas Reservoirs. *Sci. Technol. Innov. Appl.* **2017**, *14*, 165–177.
8. Zhang, P.; Wang, D.K.; Yu, C.; Zeng, C.F. The process of digital coal core construction and the characterization of crack morphology on industrial CT scanning. *J. Henan Polytech. Univ. Nat. Sci. Ed.* **2019**, *38*, 10–16. [CrossRef]
9. Wang, R.; Feng, H.; Liu, C. Applicability of mercury intrusion and liquid nitrogen adsorption methods inizing the pore structure of high-rank coal. *Oil Drill. Prod. Technol. Shiyou Zuancai Gongyi* **2024**, *46*, 25–38. [CrossRef]
10. Guo, J.; Tian, W.; Cheng, X.; Yun, W. Study on the evolution of concrete pore structure and moisture transfer mechanism after high temperature based on different sequence NMR technology. *Constr. Build. Mater.* **2024**, *422*, 135739. [CrossRef]
11. Cai, J.; Chen, J.-G.; Shi, J.; Tian, Q.; Xu, G.; Du, Y. A novel approach to evaluate the clogging resistance of pervious concrete. *Case Stud. Constr. Mater.* **2022**, *16*, 00864. [CrossRef]
12. Chai, L.; Chen, B.; Guo, L.; Ren, B.; Chen, Z.; Huang, T. Effect of Ambient Temperature on the Mechanical Properties of High Ductility Concrete. *Materials* **2023**, *16*, 2465. [CrossRef] [PubMed]
13. Yang, S.; Mao, H.; Liu, C.; Wang, X.J. Study on the Relationship Model between Compressive Strength and Pore Distribution Characteristics of Medium and High Strength Concrete. *J. Yangtze River Sci. Res. Inst.* **2024**, *41*, 194–202.
14. Cai, P.; Mao, X.; He, P.; Lai, X. Quantifying Three-Dimensional Macropore Structure and Seepage Characteristics of Representative Elementary Volume for Recycled Aggregate Pervious Concrete. *J. Mater. Civ. Eng.* **2024**, *36*, 04024092. [CrossRef]
15. Hua, C.; Tang, R.; Lu, X. Radon emission characteristics and pore structure evolution of self-compacting concrete with silica fume-molybdenum tailings under different curing environments. *J. Build. Eng.* **2024**, *97*, 110769. [CrossRef]
16. Cui, J.; He, Z.; Zhang, G.; Cai, X.; Hu, L. Rheology, mechanical properties and pore structure of sprayed ultra-high performance concrete (SUHPC) with viscosity-enhancing agent. *Constr. Build. Mater.* **2022**, *350*, 128840. [CrossRef]
17. Deng, G.; He, Y.; Lu, L.; Wang, F.; Hu, S. Pore structure evolution and sulfate attack of high-volume slag blended mortars under standard curing and steam curing. *Constr. Build. Mater.* **2023**, *363*, 129878. [CrossRef]
18. Du, S.; Zhang, Y.; Zhang, J.; Selyutina, N.; Smirnov, I.; Ma, G.; Zhang, X.; Li, B.; Miao, Y.; Liu, Y.; et al. Study on pore characteristics of recycled aggregate concrete mixed with glazed hollow beads at high temperatures based on 3-D reconstruction of computed tomography images. *Constr. Build. Mater.* **2022**, *323*, 126564. [CrossRef]

19. Jiao, C.J.; Li, X.B.; Chen, C.; Li, C. Dynamic damage constitutive relationship of high strength concrete based on fractal theory. *Explos. Shock. Waves* **2018**, *38*, 925–930. (In Chinese)
20. Shang, X.Y.; Yang, J.W.; Li, J.S. Fractal characteristics of meso-failure crack in recycled coarse aggregate concrete based on CT image. *Acta Mater. Compos. Sin.* **2020**, *37*, 1774–1784. (In Chinese)
21. *GB/T 176-2017*; Methods for Chemical Analysis of Cement. China Standard Press: Beijing, China, 2017.
22. *GB/T 8074-2008*; Testing Method for Specific Surface of Cement—Blaine Method. China Standard Press: Beijing, China, 2008.
23. *JGJ 52-2006*; Standard for Technical Requirements and Test Method of Sand and Crushed Stone (or Gravel) for Ordinary Concrete. China Architecture & Building Press: Beijing, China, 2006.
24. *JC/T721-2006*; Method for Determination of Gradation of Cement Particles, Laser Method. China Architecture & Building Press: Beijing, China, 2006.
25. *GB 8076-2008*; Concrete Admixtures. China Standard Press: Beijing, China, 2008.
26. *GB/T 8077-2008*; Test Methods for the Homogeneity of Concrete Admixtures. China Standard Press: Beijing, China, 2008.
27. *GB/T 50080-2002*; Test Method for Properties of Ordinary Concrete Mixture. China Standard Press: Beijing, China, 2002.
28. *GB/T 50081-2019*; Standard for Test Methods of Physical and Mechanical Properties of Concrete. China Standard Press: Beijing, China, 2019.
29. Ye, L.J.; Xia, X.H.; Wu, D.; Gu, Y.Q.; Kuang, Y.Z.; He, H. On the micromechanical properties of foam concrete under the combined action of freeze-thaw cycles and fatigue loads. *Concrete* **2022**, *10*, 56–61. (In Chinese)